# A Lagrangian Method for Simulating Geophysical Fluids

Patrick Haertel

*Department of Geology and Geophysics, Yale University, New Haven, Connecticut, USA*

This paper reviews the recent development of a fully Lagrangian numerical method for simulating circulations in geophysical fluids. A body of water or an atmosphere is represented as a collection of conforming fluid parcels. Parcel motions are predicted using Newtonian mechanics, and neighboring parcels are allowed to exchange momentum and/or tracers to account for unresolved circulations. Overlapping parcels in convectively unstable regions exchange vertical positions to represent effects of dry and/or moist convection. Model equations for both oceans and atmospheres are provided, and lake, ocean, and atmospheric applications completed to date are summarized. The Lagrangian method is shown to be capable of simulating general circulations in oceans and atmospheres and a variety of transient phenomena including upwelling fronts, tropical instability waves, and atmospheric convective systems.

## 1. INTRODUCTION

A Lagrangian frame of reference provides the most natural and simple way to think about and formulate most atmospheric and oceanic processes, and yet few, if any, environmental modeling centers currently employ fully Lagrangian models for predicting motions in geophysical fluids. This paper reviews work done by the author and collaborators over the past 12 years to address this problem, and in particular, to provide a simple and efficient Lagrangian numerical method for simulating circulations in oceans and atmospheres. The approach presented here, which is referred to as the "Lagrangian geophysical fluid (LGF)" method, represents a body of water or an atmosphere as a collection of conforming fluid parcels (Figure 1) and predicts the motions of individual parcels using classical physics.

There are a number of advantages to the LGF approach. First, it circumvents the need to solve partial differential equations but, instead, involves a more tractable system of ordinary differential equations that describe parcel motions.

Second, certain problems that are relatively difficult to solve in an Eulerian framework, such as avoiding spurious mixing [e.g., *Griffies et al.*, 2000], computing precise fluid trajectories, and simulating atmospheric convective systems [e.g., *Lin et al.*, 2006; *Straub and Haertel*, 2010], have simple and elegant solutions in this Lagrangian framework. Third, the LGF method takes Lagrangian thinking a step further than the more common practice of embedding Lagrangian particle models for tracers within Eulerian models that predict circulations, which has potential advantages in terms representing convective and bolus transports of tracers, and providing consistency between dynamical and tracer model components.

The LGF approach has a few key differences from related Lagrangian methods including particle-in-cell [*Harlow*, 1964], smoothed particle hydrodynamics [*Monaghan*, 1992], the Hamiltonian particle mesh method [*Frank and Reich*, 2004], the finite mass method [*Yserentant*, 1997; *Gauger et al.*, 2000], and the method of *Alam and Lin* [2008]. In particular, for the purposes of calculating pressure accelerations and surface fluxes, parcels are not thought of as points of mass, but rather, their spatial extent is factored into calculations, and parcels cannot occupy the same physical space. One advantage of this is that data void and data concentrated areas do not develop during the course of a simulation, and parcels remain regularly distributed so there
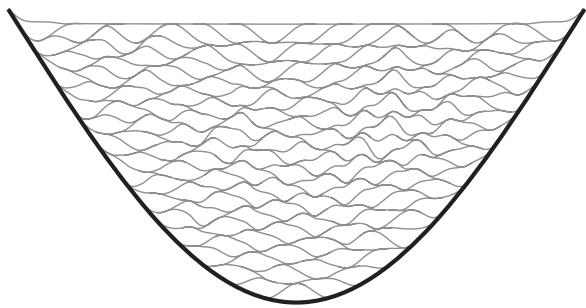
**Figure 1.** A collection of fluid parcels in a basin [from *Haertel and Fedorov*, 2012].

is no need to "remap" parcel locations as in some other Lagrangian approaches.

The LGF method has already been applied in a number of contexts: idealized fluids [*Haertel and Randall*, 2002], large lakes [*Haertel et al.*, 2004], oceans [*Haertel et al.*, 2009; *Van Roekel et al.*, 2009; *Haertel and Fedorov*, 2012], and atmospheres [*Haertel and Straub*, 2010]. In general, these studies have found that the LGF approach produces circulations similar to those generated by more conventional approaches, but with a few key differences owing to the lack of spurious numerical mixing and unique representations of moist convection and bolus transports. There is reason to believe the LGF method soon will also be used for climate simulations and numerical weather prediction; in particular, the development of a global Lagrangian atmospheric model is now underway.

This paper is organized as follows. Section 2 describes the LGF method including model equations, representation of subparcel scale circulations, and convective parameterization. Section 3 discusses tests of the LGF method on idealized fluids. Section 4 reviews lake and ocean applications completed to date. Section 5 discusses initial atmospheric results, and Section 6 is a summary and discussion.

## 2. THE LGF METHOD

This section provides equations for LGF models for both oceans and atmospheres; the two differ in the information stored for each fluid parcel and in the calculation of the pressure acceleration of parcels.

### 2.1. Parcels

The term "parcel" is used to refer to a mass of fluid that is contained in an imaginary sack and which maintains its integrity as it moves around in the fluid. In addition to the global variables for parcel radii and mass, just a few variables fully characterize a parcel: $\mathbf{x}$, $\mathbf{v}$, $T$, $S$ for ocean parcels, and $\mathbf{x}$, $\mathbf{v}$, $\theta$ for atmospheric parcels where $\mathbf{x}$ is the horizontal position, $\mathbf{v}$ is the

horizontal velocity, $T$ is the temperature, $S$ is the salinity, and $\theta$ is the potential temperature. Each parcel is assumed to have a time-invariant vertical-thickness distribution

$$H(x',y') = H_{max}p\left(\frac{|x'|}{r_x}\right)p\left(\frac{|y'|}{r_y}\right), \qquad (1)$$

where $H_{max}$ is the parcel's maximum vertical thickness (in units of height for water parcels and pressure for air parcels), $r_x$ and $r_y$ are the parcel radii in the $x$ and $y$ directions, the prime (′) notation denotes a coordinate system centered on the parcel, and $p(x) = 1 + (2x - 3)x^2$ for $x < 1$. Note that the vertical thickness function is bell-shaped (Figures 2a and 2b), but that parcels have a variety of shapes because they conform to surfaces beneath them, leaving no gaps between parcels (Figures 1 and 2c). While the LGF approach can work with a variety of vertical thickness functions, a product of third-order polynomials is used in equation (1) for computational efficiency [*Haertel et al.*, 2004].

For atmospheric applications, a parcel's maximum vertical thickness, $H_{max}$, is defined as a pressure difference between
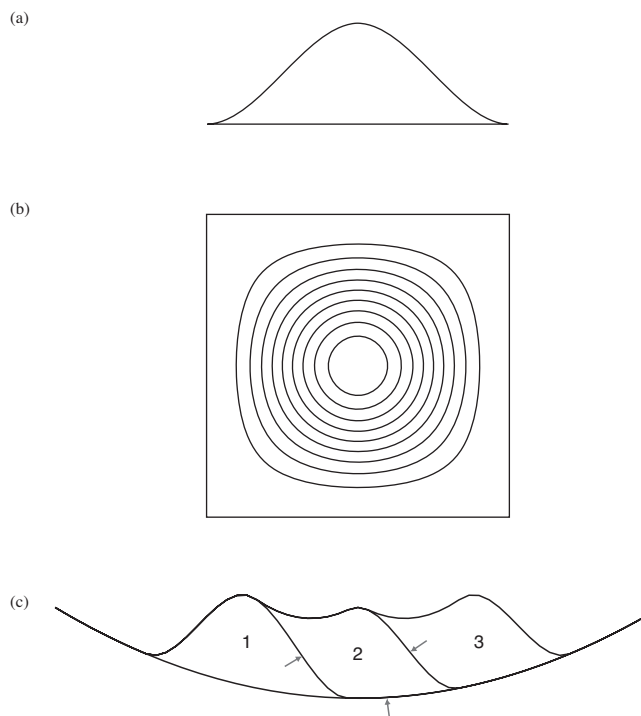
(a)

(b)

(c)



**Figure 2.** Parcel shapes, deformations, and the pressure force. (a) Profile of a parcel on a level surface. (b) Top-down view of the parcel with contours shown for 0.0, 0.1, . . ., 0.9 times the maximum vertical thickness. (c) Three parcels in a basin, numbered according to their stacking order, with vectors indicating the contributions to the pressure force on parcel 2 from the other parcels and the bottom topography.

the top and bottom of the parcel, and it is held constant during a model run. For oceanic applications, a parcel's maximum vertical thickness, $H_{max}$, has units of meters and is determined as follows:

$$H_{max} = \frac{m}{\rho r_x r_y},\qquad(2)$$

where $m$ is the parcel mass and $\rho$ is the parcel density, which is diagnosed after each time step with an equation state for water. In other words, for ocean applications, a parcel's mass is held constant but its vertical thickness changes slightly owing to variations in density.

Despite the complexity of parcel shapes shown in Figure 1, it is relatively easy to specify them mathematically. The following formula defines the height $z$ of the upper surface of the $k$th parcel for the ocean model:

$$z(\mathbf{x}) = \sum_{i=1}^{k} H_i(\mathbf{x} - \mathbf{x}_i) + b(\mathbf{x}),\qquad(3)$$

where $b$ is the height of the bottom topography. Similarly, the pressure $p$ on the upper surface of the $k$th parcel for the atmospheric model is

$$p(\mathbf{x}) = \sum_{i=k+1}^{n} H_i(\mathbf{x} - \mathbf{x}_i),\qquad(4)$$

where $n$ is the total number of parcels. In practice, parcel interfaces are not tracked, however; rather, only the minimal information needed to calculate the net pressure acceleration of each parcel is used (see below).

One important consequence of the way that parcels are defined, as having a spatial extent as opposed to being points of fluid, is that they tend to remain fairly uniformly distributed during the course of a simulation. This happens because when parcels begin to evacuate a given region, pressure forces induce a convergence of mass, which is analogous to what happens in real fluids. This means that there is no need to repartition fluid into parcels during the course of a simulation, although in some circumstances, repartitioning can be done to enhance computational efficiency (e.g., to allow a variable resolution) [*Haertel and Fedorov*, 2012].

### 2.2. Equations of Motion

The equations of motion for an individual parcel are as follows:

$$\frac{d\mathbf{x}}{dt} = \mathbf{v}\qquad(5)$$

$$\frac{d\mathbf{v}}{dt} + f\mathbf{k} \times \mathbf{v} = \mathbf{A}_p + \mathbf{A}_m,\qquad(6)$$

where $t$ is time, $f$ is the Coriolis parameter, $\mathbf{k}$ is the unit vector in the vertical, $\mathbf{A}_p$ is the horizontal acceleration of the parcel resulting from pressure, and $\mathbf{A}_m$ is the horizontal acceleration of the parcel resulting from parameterized turbulent mixing of momentum. Whereas parcels' horizontal positions are explicitly predicted, vertical positions are implicitly determined by the parcels' positioning in the pile. Initially, we used third-order Adams-Bashforth time differencing to approximate the time derivatives in equations (5)–(6), but more recently, we have used a version of leapfrog time differencing with implicit treatment of Coriolis terms, which requires less data storage and allows longer time steps.

### 2.3. The Pressure Acceleration

The pressure acceleration ($\mathbf{A}_p$) has a different form for oceans and atmospheres, which reflects the difference in the compressibilities of water and air, and the assumptions that density is spatially uniform within a water parcel and potential temperature is spatially uniform within an air parcel. In both cases, pressure is assumed to be hydrostatic.

For oceans, the pressure acceleration is as follows [*Haertel and Randall*, 2002; *Haertel et al.*, 2009]:

$$\mathbf{A}_{p_i} = \frac{1}{m_i}\int g\nabla H_i\left[\sum_{j=i+1}^{n}(\rho_j - \rho_i)H_j + \rho_i\left(b + \sum_{j=1}^{n} H_j\right)\right]d\mu,\quad(7)$$

where the integral is evaluated over the horizontal projection of parcel $i$, $g$ is gravity, $n$ is the total number of parcels, and $d\mu$ is the horizontal area measure. Equation (7) was obtained by integrating pressure times the inward normal vector over the surface of the parcel, taking the horizontal projection of the net force vector and integrating by parts [*Haertel and Randall*, 2002]. Note that both the slope of the parcel surface and the weight of the parcels above contribute to the acceleration, which is why thicknesses of both parcels below (with indices less than $i$) and parcels above (with indices greater than $i$) affect this force. Figure 2c illustrates such contributions graphically for a particular parcel in a three-parcel system. Parcel 1 pushes upward and to the right on parcel 2, parcel 3 pushes downward and to the left on parcel 2, and the bottom topography pushes upward and slightly to the left on parcel 2.

The integral in equation (7) is typically approximated with a Riemann sum, which leads to the conservation of energy in the limit as the time step approaches zero and requires $O(n)$ operations to evaluate for $n$ parcels [*Haertel and Randall*, 2002; *Haertel et al.*, 2004]. In most oceanic applications, a form of gravity wave retardation [*Jensen*, 1996] is used to slow external gravity waves by a factor of 3–10 [e.g., *Haertel et al.*, 2004; *Van Roekel et al.*, 2009; *Haertel and Fedorov*,

2012]. This amounts to assuming that rather than displacing air, water parcels displace a fluid with a density that is 90%–99% the average density of the water. This fluid is represented in equation (7) as the $n$th parcel, and it is assumed to have a perfectly level free surface.

For atmospheres, the pressure force is as follows [*Haertel and Straub*, 2010]:

$$\mathbf{A}_p = \frac{1}{W}\int \nabla HM \,\mathrm{d}\mu,$$

where the integral is evaluated over the horizontal projection of the parcel, $M = C_pT + gz$ is the Montgomery potential or dry static energy, and $W$ is the parcel weight. At the surface, $M$ is set to $gz$ (i.e., $T$ is defined to be zero), and the change in the Montgomery potential (d$M$) rising vertically across a parcel interface is given by d$M = C_p$d$T$, where the pressure at the interface equals the sum of the pressure thickness functions above it, and the temperature $T$ is calculated from the potential temperature using Poisson's equation. Note that there are no approximations resulting from this vertical discretization, which is a consequence of the fact that the Montgomery potential is independent of height within an isentropic layer.

### 2.4. Unresolved Momentum Transport ($\mathbf{A}_m$)

Parcels are allowed to exchange momentum with their nearest neighbors in order to represent transport by subparcel-scale circulations. This process essentially equates to including both horizontal and vertical eddy viscosities, and it is implemented in the following manner. First, parcel centers are partitioned into rows and columns that run parallel to each coordinate axis, where density or potential temperature is used for a vertical coordinate. Then, each row or column of parcel centers is treated like a row or column of points in an Eulerian finite difference model. In other words, a flux of momentum or density is calculated between each parcel and its nearest neighbors in each mixing row or column that it is contained in. For more details on the implementation of vertical and horizontal diffusion, the reader is referred to the works of *Haertel et al.* [2004] and *Haertel et al.* [2009], respectively.

### 2.5. Convective Parameterization

The Lagrangian ocean and atmosphere models include a convective parameterization in which overlapping parcels in convectively unstable regions exchange vertical positions. This Lagrangian overturning (LO) is applied to one column of parcels at a time beginning with the lowest pair of parcels (Figure 3a). A test is performed to see if swapping parcel
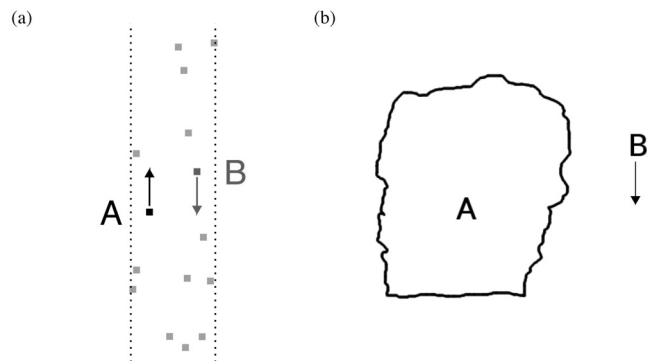


**Figure 3.** The Lagrangian overturning convective parameterization [from *Haertel and Straub*, 2010]. (a) A column of parcel centers from an actual Lagrangian simulation. Points A and B satisfy the check for the convective parameterization, exchanging their vertical positions leads to a higher potential temperature (or lower potential density) for the rising parcel. (b) The physical processes the swap parameterizes: parcel A represents air rising in convective clouds, and parcel B represents air sinking around the clouds.

vertical positions leads to a lower density (or higher potential temperature) for the rising parcel, in which case the vertical swap is performed. In atmospheric applications, the heat released from condensation of excess water vapor is factored into the calculation [*Haertel and Straub*, 2010]. The LO convective parameterization is intended to represent both the vertical motion in convective updrafts/downdrafts and the compensating flow around them (Figure 3b). In atmospheric applications, LO has been shown to generate realistic convective systems (Section 5).

## 3. SIMULATIONS OF IDEALIZED FLUIDS

Prior to its application to oceans and atmospheres, the LGF method was used to model circulations in idealized fluids [*Haertel and Randall*, 2002]. Several such simulations are discussed in this section, which show that in many respects, piles of conforming parcels behave like fluids.

The following is a simple illustration of how gravity waves propagate through conforming parcels much like they do through continuous fluids. Consider a pile of 10 fluid parcels in a basin, and suppose a positive momentum perturbation is introduced to the interior parcels (Figure 4a). With time, the perturbed parcels move toward the right, converging mass on the right side of the momentum perturbation and diverging mass on the left side (Figure 4b). The resulting pressure gradient reduces the momentum perturbation in the center but enhances it to the left and the right (Figure 4b). Over time, the momentum perturbation divides in two, with each half propagating away as an external gravity wave (Figure 4c). The
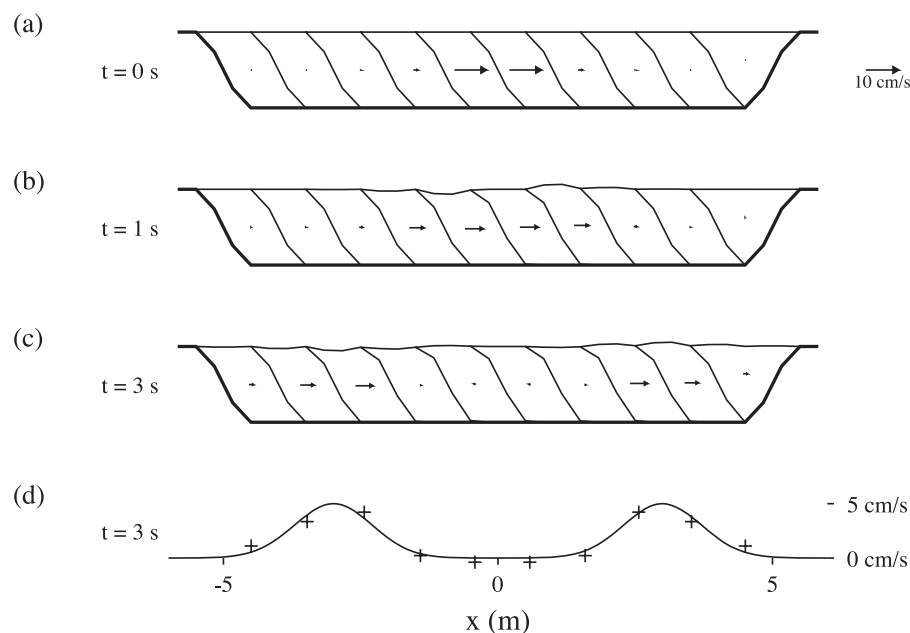
**Figure 4.** Gravity waves propagating through parcels in a basin. (a–c) Parcel outlines and velocities for $t = 0, 1, 3$ s, respectively. (d) Parcel velocities (crosses) and velocity for the corresponding problem in a continuous fluid (black line) for $t = 3$ s. To make the solution comparable to that for nondimensional shallow water equations, the initial depth is set to 1 m and the value for gravity used is $1 \text{ m s}^{-2}$.

corresponding velocity for the same experiment in a continuous fluid is shown in Figure 4d. Despite the fact that the momentum perturbation is resolved by only a couple of parcels, external gravity waves propagate through the discrete system much like those in the continuous fluid. Moreover, as the number (size) of the parcels is increased (decreased), the solution converges toward that of a continuous fluid (not shown).

*Haertel and Randall* [2002] performed a similar experiment to that shown in Figure 4, but which included a second fluid layer and involved both external and internal gravity waves. They also carefully examined numerical convergence to the behavior of a continuous fluid and found differences to be proportional to the second power of the parcel width when the parcel aspect ratio was held constant. They also found that Rossby waves propagate through piles of parcels much like they do through continuous fluids and that the LGF method can be used to reproduce the nonlinear analytic solution for a 2-D spreading ridge of fluid [*Frei*, 1993; *Schar and Smolarkiewicz*, 1996].

## 4. LAKE AND OCEAN APPLICATIONS

After the LGF approach was tested for idealized fluids, it was used to simulate circulations in large lakes and idealized oceans; these applications are reviewed in this section.

### 4.1. Large Lake Upwelling

The first 3-D application of the LGF method was simulating upwelling in an idealized large lake [*Haertel et al.*, 2004]. This test case was selected because it is a simple example of the response of a body of water to a surface wind-stress forcing, but still involves some interesting physics and dynamics including variable bottom topography, internal gravity waves, boundary currents, topographic waves, shear-dependent vertical mixing, and convective adjustment. *Haertel et al.* [2004] compared Lagrangian simulations of lake upwelling to similar simulations conducted with $z$  and σ coordinate ocean models by *Beletsky et al.* [1997]. In general, the Lagrangian ocean model (LOM) produced circulations much like those in the other models, including upwelling fronts and topographic waves, but it generated less mixing across the thermocline (Figure 5). For example, water that upwelled on the eastern boundary had the same temperature as deep water in the LOM (Figure 5a), but a higher temperature owing to mixing in the Princeton ocean model (POM) (Figure 5b). Differences in temperature extremes became more pronounced with time, after upwelling fronts propagated cyclonically around the lake separating the coldest water from the shoreline (Figures 5c and 5d). In the LOM, the temperature extremes were maintained over this time (Figure 5c), but in the POM, the upwelled water warmed, despite the fact that there was no surface temperature
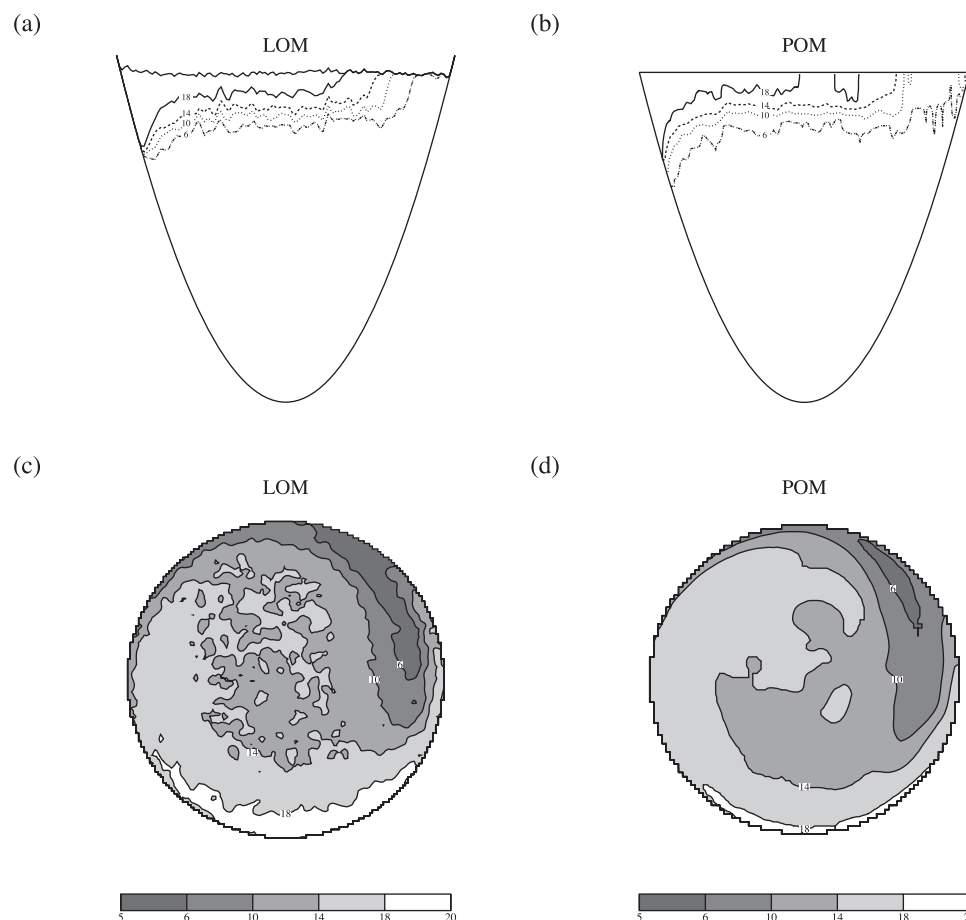
**Figure 5.** Comparison of lake upwelling simulations conducted with the Lagrangian ocean model (LOM) and the Princeton ocean model (POM) [from *Haertel et al.*, 2004; *Beletsky et al.*, 1997]. The lake was exposed to strong northerly winds for approximately 1 day. (a–b) East-west cross sections of temperature (°C) at 29 h for LOM and POM simulations, respectively. Notice that the thermocline is more diffuse in the POM simulation. (c–d) Horizontal cross sections of temperature (°C) at 10 m at 5 days for LOM and POM simulations, respectively, which show propagation of upwelling fronts and topographic waves.

forcing (Figure 5d). This difference is expected because the POM is subject to spurious numerical mixing of tracers [e.g., *Griffies et al.*, 2000], whereas the LOM has none. The computational efficiency of the LOM was compared to that of the POM for the lake upwelling simulations, and after a number of steps were taken to optimize the LOM, its efficiency became competitive with the POM [*Haertel et al.*, 2004].

### 4.2. Equatorial Oceans

The second oceanic application of the LGF method was simulating circulations in idealized equatorial oceans using the configuration developed by *Boccaletti et al.* [2004] and *Fedorov et al.* [2004]. These simulations were presented at the 14th Ocean Sciences meeting in Orlando, FL, in February 2008. The oceans were 40°–80° wide, about 32° in meridional extent, and centered on the equator. They were exposed to surface easterlies and a temperature restoring that included cooling near the northern and southern boundaries [*Boccaletti et al.*, 2004]. Model resolutions varied from 0.5° to 1.5°. The zonal current structure for one such LOM simulation is compared to that for a *z* coordinate ocean model in Figures 6a–6d. The LOM generated realistic surface current and equatorial undercurrent structure (Figures 6a and 6b), as well as a sloping thermocline much like that generated by the *z* coordinate ocean model (not shown).

One feature of the LOM simulations of equatorial oceans that was particularly impressive is their representations of tropical instability waves (TIWs), which developed at surprisingly low resolution. For example, Figures 6c–6e show
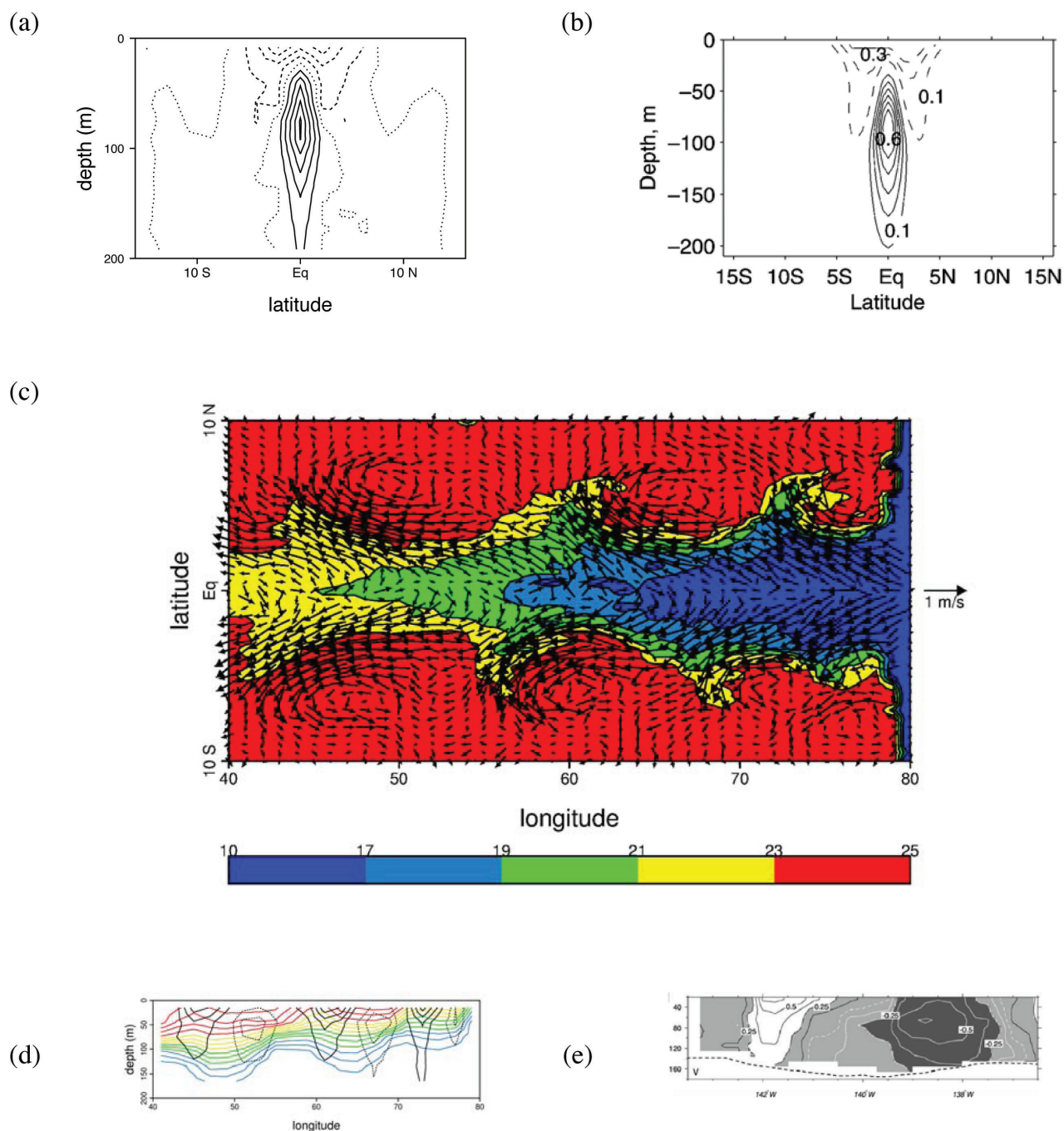
(a)

(b)

(c)



(d)

(e)

**Figure 6.** Lagrangian simulations of idealized equatorial oceans. (a) North-south cross section of zonal velocity (0.1 m s$^{-1}$ contour interval). (b) As in Figure 6a but for a height coordinate ocean model [from *Fedorov et al.*, 2004]. (c) Surface temperature and velocity for a Lagrangian simulation with robust tropical instability waves (TIWs). (d) Vertical structure of meridional velocity (black lines) and temperature (colored lines) for simulated TIWs. (e) Observed vertical structure of meridional velocity for a TIW vortex [from *Kennan and Flament*, 2000].

TIWs simulated in an 80° wide equatorial ocean using a parcel radius of 1.5°. Strong cusps in surface temperature are present (Figure 6c) associated with tropical instability wave vortices that have realistic 3-D structure (Figures 6d and 6e) (observations from *Kennan and Flament* [2000]). Moreover, because TIWs are believed to involve both barotropic and baroclinic instabilities [e.g., *Grodsky et al.*, 2005], this result provides evidence that the LGF approach properly simulates these instabilities.

### 4.3. Atlantic/Southern Oceans

Recently, the LGF method has been used in a series of studies of the Atlantic and Southern Oceans to both test its capacity to simulate ocean circulations and to address several scientific questions well suited to a Lagrangian framework.

*Haertel et al.* [2009] constructed an idealized model of the North Atlantic and compared Lagrangian simulations of thermocline structure and subtropical gyres to similar simulations carried out with a *z*-coordinate ocean model. They found that when moderate mixing was employed, the Lagrangian and *z*-coordinate model produced nearly identical thermocline structure (Figure 7), with minor differences near boundaries owing to differing slopes in basin walls. They also showed that the LGF approach could reproduce Munk and Stommel solutions to the classical western boundary current problem.

*Van Roekel et al.* [2009] used the LGF method to study the sensitivity of the deep meridional overturning circulation to the location of diapycnal mixing. They verified that strong vertical transports at depth occur only in regions of strong mixing. They also isolated the potential impact of vertical mixing by tropical cyclones and quantified its effects on Atlantic heat transport.
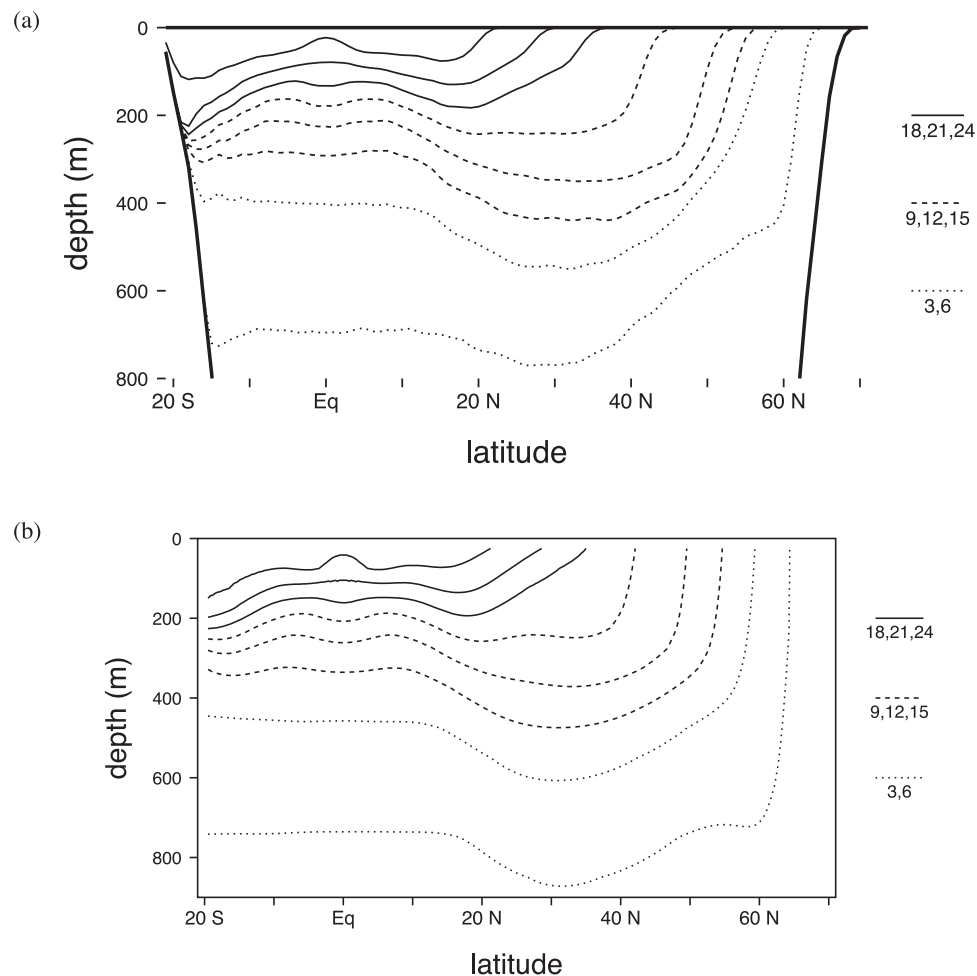


**Figure 7.** A comparison of Atlantic thermocline structure generated by the LOM and a *z*-coordinate ocean model [from *Haertel et al.*, 2009]. (a) Temperature (°C) along 30°W for the LOM. (b) Temperature (°C) along 30°W for the *z*-coordinate ocean model.

*Haertel and Fedorov* [2012] examined ocean stratification and overturning in the limit of zero interior diffusion for an ocean basin that included approximate forms of the Atlantic and Southern Oceans. Their model reproduced the gross stratification and water mass distribution observed in the Atlantic Ocean in the adiabatic limit (Figure 8). This study provided several examples of advantages of using a Lagrangian approach for fluid modeling. First, it addressed a scientific question that cannot be fully addressed in an Eulerian framework because of spurious numerical mixing [*Griffies et al.*, 2000]. Second, it took advantage of the fact that trajectories were provided for every parcel in the ocean with no additional computational cost. For example, Figure 8b shows the latitude at which each parcel last had contact with the surface, which not only explains the interior density structure (Figure 8a), but also allows for an identification of water masses that can be compared with those observed in nature (Figure 8c). Finally, the simulations conducted by *Haertel and Fedorov* [2012] demonstrated some unique behavior of Lagrangian models in terms of bolus transports. When run at low resolution, Eulerian ocean models typically use the Gent-Mcwilliams (GM) parameterization to represent the effects of subgrid-scale eddies [*Gent and Mcwilliams*, 1990], which make important contributions to both overturning and stratification [e.g., *Marshall and Radko*, 2003]. However, it was found that the LOM spontaneously generated such bolus transports owing to chaotic deviations of individual parcel trajectories from the mean flow [see *Haertel and Fedorov*, 2012, Figure 13], so that there was no need to use a GM parameterization to generate realistic overturning and stratification structure.

## 5. INITIAL ATMOSPHERIC RESULTS

While the majority of the simulations conducted using the LGF method have been for oceans, recently, the approach also has been applied to atmospheres with encouraging results.

*Haertel and Straub* [2010] constructed a tropical aquaplanet model using the LGF method and examined the organization of convective systems. They used a prescribed, zonally symmetric sea surface temperature (SST) that was an analytic approximation of the observed SST over the western Pacific. Their simulations generated robust convectively coupled equatorial Kelvin waves, with realistic horizontal (Figure 9a) and vertical structures (Figures 9b and 9c). This result is particularly encouraging because few climate models adequately simulate equatorial Kelvin waves [*Straub and Haertel*, 2010], and it is attributed to the unique LO convective parameterization (Figure 3).

Ongoing work suggests that the LO convective scheme also can be used to simulate robust Madden-Julian oscillations (MJOs) [*Madden and Julian*, 1972, 1994; *Zhang*, 2005]. The MJO has global impacts on weather and climate with feedback on hurricanes [*Maloney*, 2000; *Barrett and Leslie*, 2009], El Niño–Southern Oscillation [*McPhaden*, 2004; *Hendon et al.*, 2007], and Asian and North American monsoons [*Wu et al.*, 1999; *Lorenz and Hartmann*, 2006], and yet the MJO has been inadequately represented in conventional climate models for decades [e.g., *Lin et al.*, 2006]. However, we recently discovered that when the vertical position swaps of LO (Figure 3a) are subcycled so that they occur many times per dynamics time step, strong MJOs can form. For example, Figure 10a shows time series of equatorial precipitation for an aquaplanet simulation using an annual Levitus climatology for SST zonally interpolated over continental locations. Slow-moving (~5 m s$^{-1}$) planetary-scale convective disturbances develop that originate in the Indian Ocean and dissipate near the International Date Line and have periods of about 50 days. Comparing their horizontal and vertical structures with those observed for the MJO (Figures 10b–10e) reveals excellent agreement.

While the initial focus of LGF aquaplanet simulations has been on tropical convective organization, other aspects of the simulations appear to be reasonable as well. For example, Figure 11 compares simulated zonal wind and precipitation patterns for the MJO simulation shown in Figure 10 with observationally based estimates. Despite the fact that the Lagrangian atmospheric model is highly idealized, with no continents, truncated meridional boundaries, and very low resolution, it produces zonal jets (Figure 11a), low-level tropical easterlies (Figure 11a), and a gross precipitation pattern (Figure 11c) that are broadly in line with observations (Figures 11b and d). While the upper tropospheric tropical westerly flow (i.e., superrotation) is unrealistic, the presence of strong and persistent MJOs (Figure 10) may contribute to this feature [*Caballero and Huber*, 2010].

## 6. SUMMARY AND DISCUSSION

This paper reviews the recent development of a Lagrangian numerical method for simulating large-scale circulations in lakes, oceans, and atmospheres. A body of water or an atmosphere is represented as a pile of conforming parcels whose motions are predicted using classical physics. Neighboring parcels are allowed to exchange mass or momentum to account for unresolved circulations, and overlapping parcels in convectively unstable regions exchange vertical positions to represent unresolved convection.

The LGF approach has been applied in a number of ways: to idealized fluids, to lakes and oceans, and in atmospheric
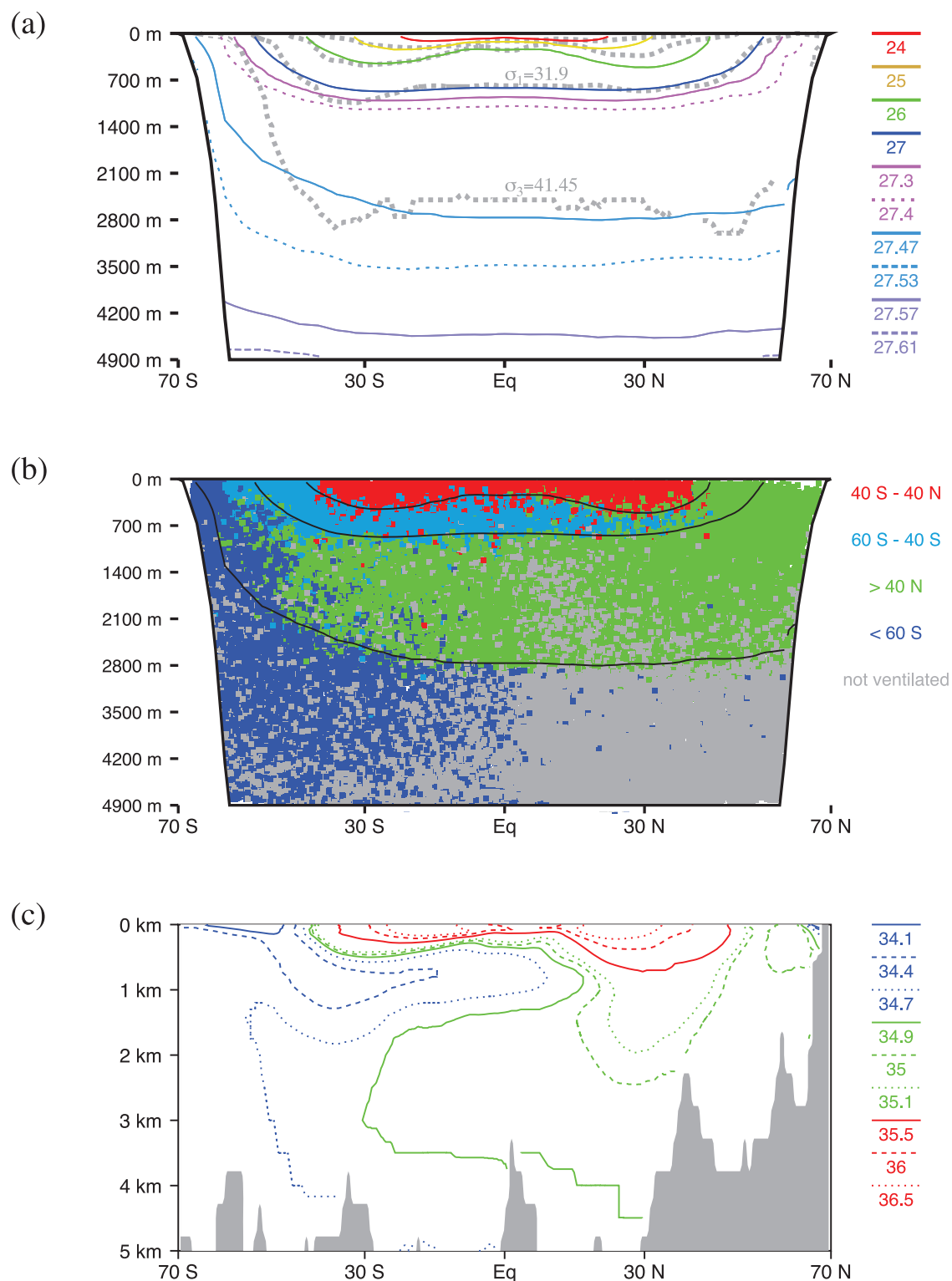
**Figure 8.** Ocean density and water masses for an ocean with an adiabatic interior [from *Haertel and Fedorov*, 2012]. (a) Simulated density along 30°W (colored contours), along with observed isopycnals (dashed gray lines) for $\sigma_0 = 26$, 26.7, $\sigma_1 = 31.9$, and $\sigma_3 = 41.45$ (where $\sigma_n$ is potential density referenced to $n \times 1000$ dbar). (b) Water parcels shown as small squares colored according to the latitude at which they last had contact with the surface (showing different water masses). Black contours mark the 1026, 1027, and 1027.47 kg m$^{-3}$ isopycnals. Parcels shaded gray were not ventilated during the last 700 years of the simulation; bottom water north of the equator primarily comprises such parcels. (c) Observed (Levitus) salinity along 30°W (psu). Note that the LOM produces a northward intrusion of Antarctic Intermediate Water similar to that in nature.
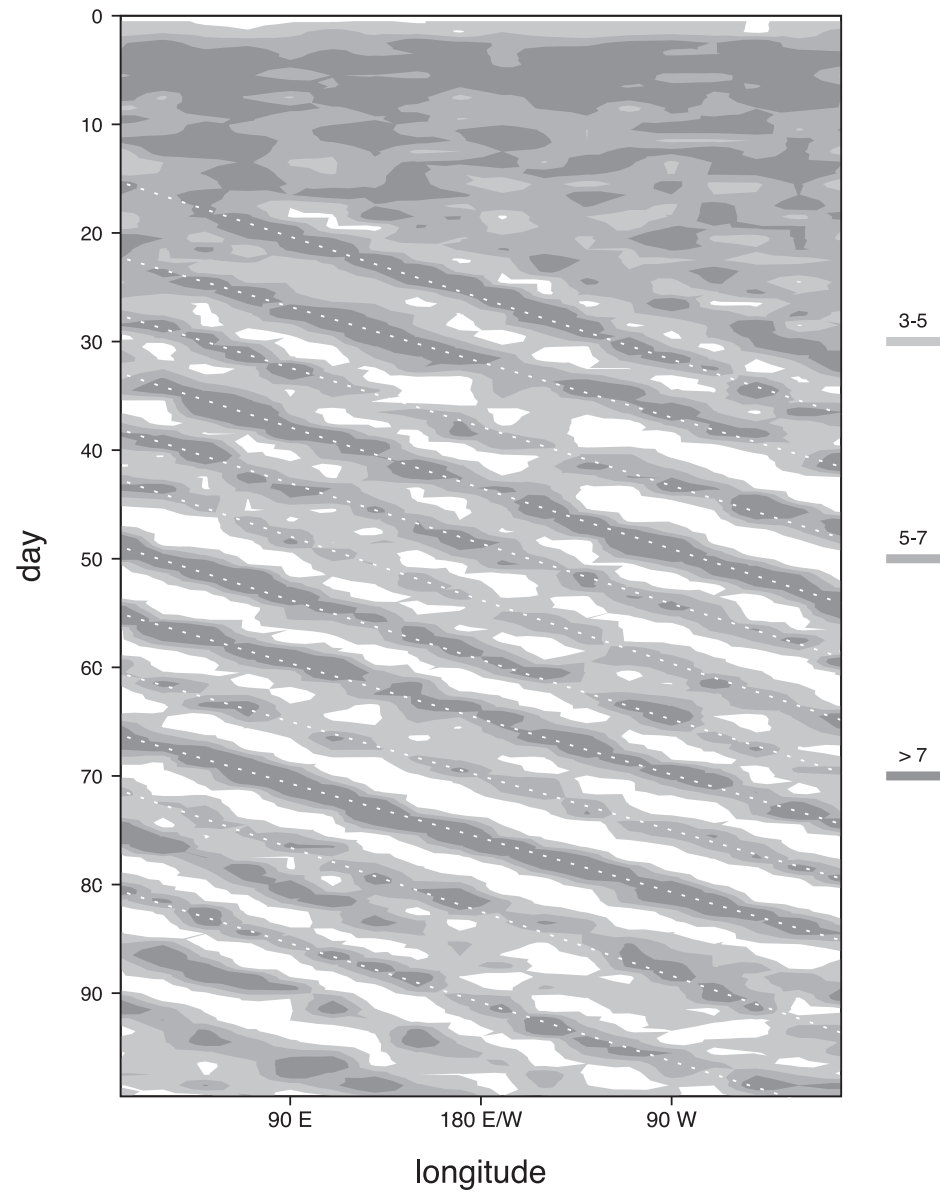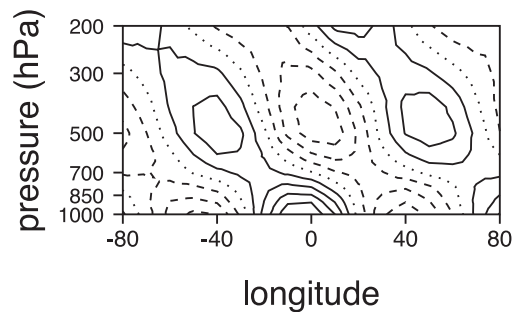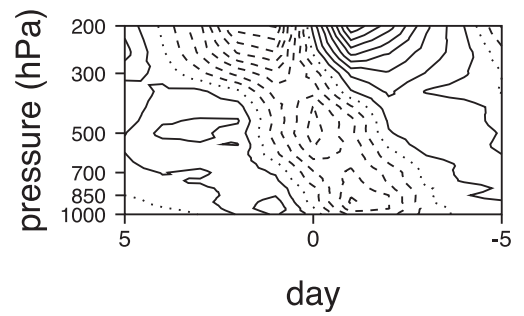
**Figure 9.** Convectively coupled Kelvin waves in a Lagrangian aquaplanet simulation [from *Haertel and Straub*, 2010]. (a) Time pressure series of rainfall (mm d$^{-1}$) averaged from 15°S to 15°N. Approximate paths of long-lived Kelvin waves are marked with dotted lines. (b and c) Composite vertical structures of zonal wind for simulated and observed Kelvin waves, respectively. The contour interval is 1 m s$^{-1}$ for Figure 9b and 0.5 m s$^{-1}$ for Figure 9c.

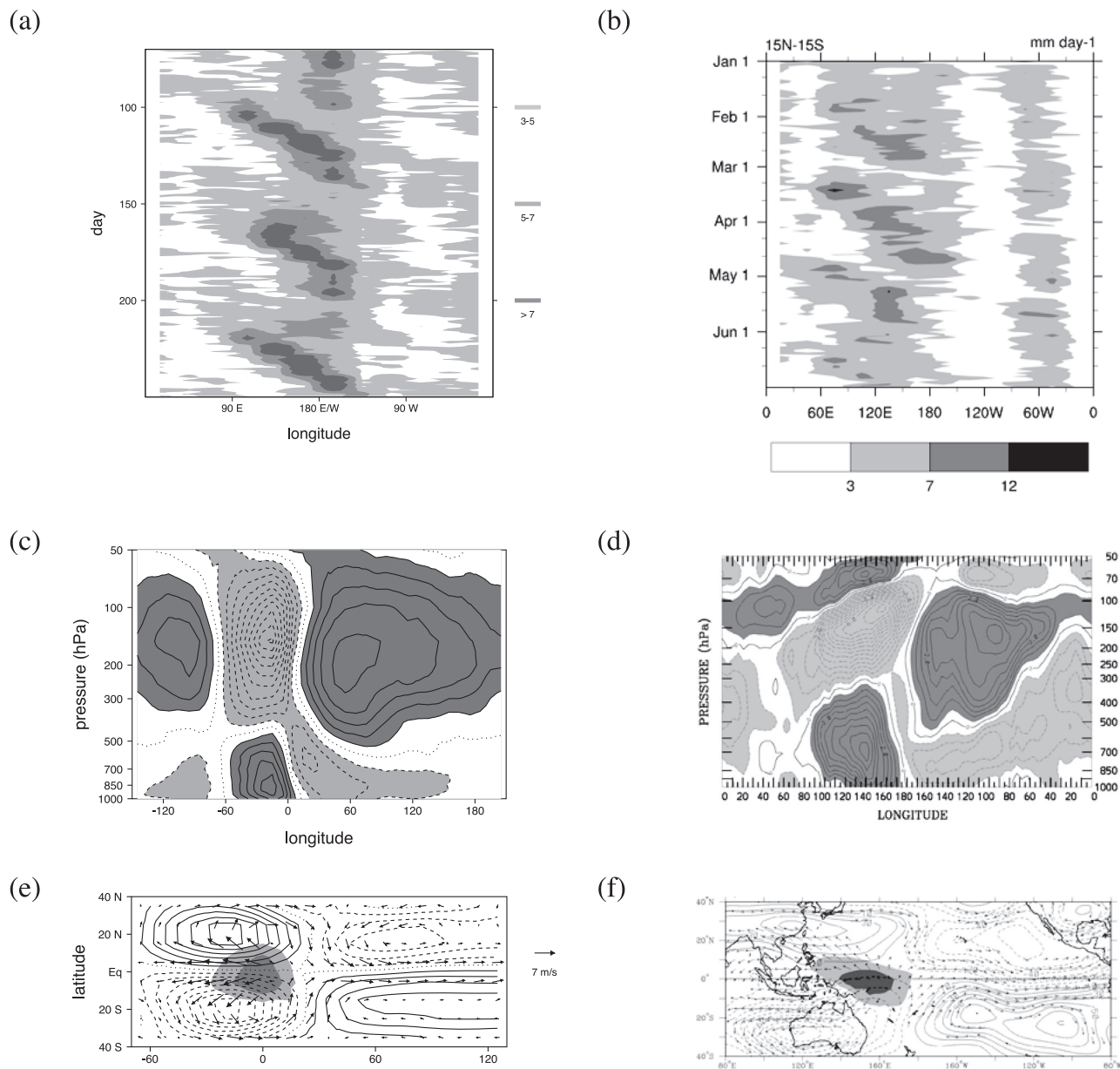(a)

(b)



(c)

(d)



(e)

(f)



**Figure 10.** Comparison of (left) simulated and (right) observed Madden-Julian Oscillations (MJO). (a–b) Time longitude series of rainfall (mm d$^{-1}$). (c and d) Vertical cross sections of zonal wind (1 and 0.5 m s$^{-1}$ contour intervals, respectively). (e and f) The 200 hPa flow and streamlines, with regions of enhanced rainfall/cloudiness shaded. Figures 10a and 10b provide examples of particular simulated and observed MJO events, respectively. The observational composites (Figures 10d and 10f) are constructed using linear regression with MJO-filtered outgoing longwave radiation at a fixed location using many years of data [*Kiladis et al.*, 2005]. The simulated composites (Figures 10c and 10e) are constructed by tracking the three MJOs shown in Figure 10a and computing their average structure in a coordinate system moving with the MJO.

simulations. In general, LGF models generate circulations that are similar to those produced by Eulerian models, but with a few differences owing to the lack of spurious numerical mixing, and unique representations of convection and bolus transports. For example, realistic convec-

tively coupled equatorial waves and MJO spontaneously form in LGF atmospheric models owing to the LO convective parameterization (Figures 9 and 10), whereas these disturbances are more challenging to simulate with Eulerian models [e.g., *Straub et al.*, 2010; *Lin et al.*, 2006].
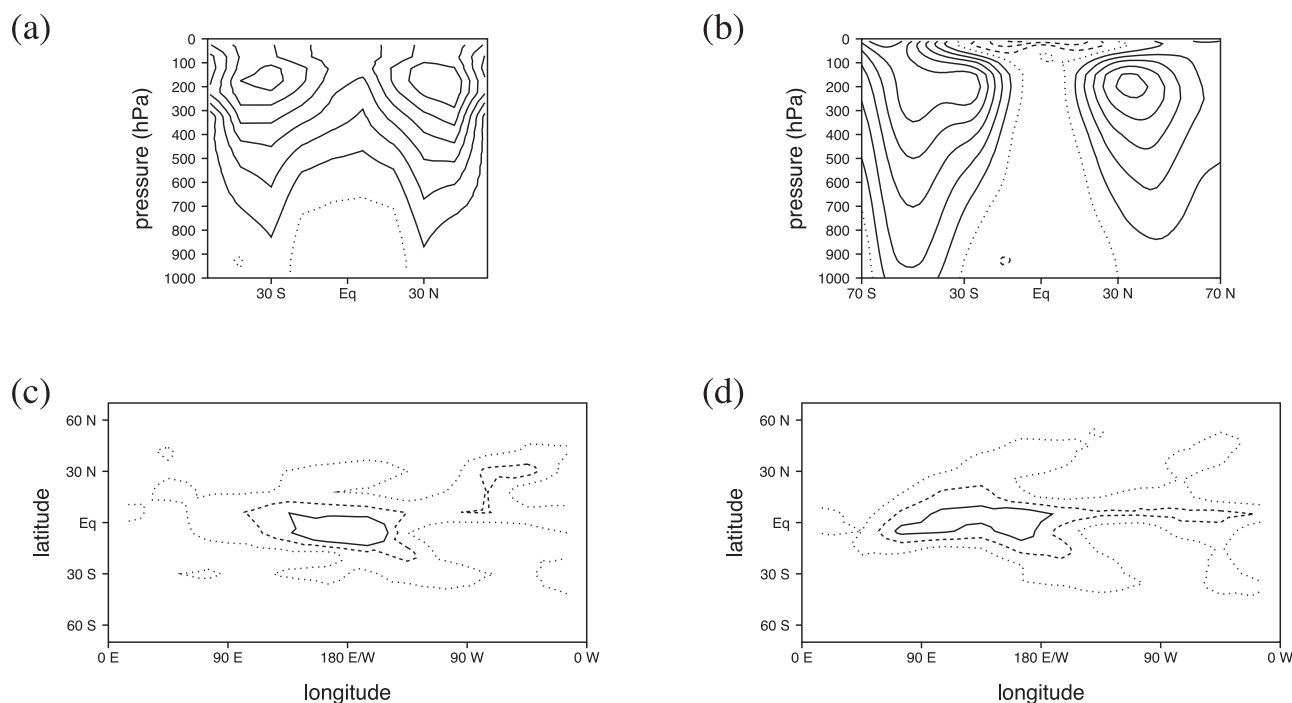
(a)

(b)

(c)

(d)

**Figure 11.** Basic state flow and precipitation for the Lagrangian MJO (left) simulation and (right) observations. (a and b) Zonal mean zonal wind (5 m s$^{-1}$ contour interval). (c and d) precipitation (three (dotted), five (dashed), and seven (solid) mm d$^{-1}$ contours are shown). The observed zonal wind field (Figure 11b) is from National Centers for Environmental Prediction Reanalysis, and the observed precipitation is from the Global Precipitation Climatology Project data set.

Moreover, LGF ocean simulations spontaneously generate robust tropical instability waves (Figure 6), even at a low horizontal resolution.

There is reason to believe that the LGF approach will have numerous future applications, particular in the areas of weather and climate simulations. Using the LGF method to track tracers might also have advantages over the more common approach of embedding particle models within Eulerian models that predict circulations because the LO convective parameterization and Lagrangian bolus transports might disperse tracers like the unresolved circulations do in nature. For these reasons, the development of a global Lagrangian atmospheric model is currently underway.

## REFERENCES

Alam, J. M., and J. C. Lin (2008), Toward a fully Lagrangian atmospheric modeling system, *Mon. Weather Rev.*, *136*, 4653–4667.

Barrett, B. S., and L. M. Leslie (2009), Links between tropical cyclone activity and Madden-Julian Oscillation Phase in the North Atlantic and Northeast Pacific basins, *Mon. Weather Rev.*, *137*, 727–744.

Beletsky, D., W. P. O'Connor, D. J. Schwab, and D. E. Dietrich (1997), Numerical simulation of internal Kelvin waves and coastal upwelling fronts, *J. Phys. Oceanogr.*, *27*, 1197–1215.

Boccaletti, G., R. C. Pacanowski, S. G. H. Philander, and A. V. Fedorov (2004), The thermal structure of the upper ocean, *J. Phys. Oceanogr.*, *34*, 888–902.

Caballero, R., and M. Huber (2010), Spontaneous transition to superrotation in warm climates simulated by CAM3, *Geophys. Res. Lett.*, *37*, L11701, doi:10.1029/2010GL043468.

Fedorov, A. V., R. C. Pacanowski, S. G. Philander, and G. Boccaletti (2004), The effect of salinity on the wind-driven circulation and the thermal structure of the upper ocean, *J. Phys. Oceanogr.*, *34*, 1949–1966.

Frank, J., and S. Reich (2004), The Hamiltonian particle mesh method for the spherical shallow-water equations, *Atmos. Sci. Lett.*, *5*, 89–95.

Frei, C. (1993), Dynamics of a two-dimensional ribbon of shallow water on an f-plane, *Tellus, Ser. A*, *45*, 44–53.

Gauger, C., P. Leinen, and H. Yserentant (2000), The finite mass method, *SIAM J. Numer. Anal.*, *37*, 1768–1799.

Gent, P. R., and J. C. Mcwilliams (1990), Isopyncal mixing in ocean circulation models, *J. Phys. Oceanogr.*, *20*, 150–155.

Griffies, S. M., R. C. Pacanowski, and R. W. Hallberg (2000), Spurious diapycnal mixing associated with advection in a z-coordinate ocean model, *Mon. Weather Rev.*, *128*, 538–564.

Grodsky, S. A., J. A. Carton, C. Provost, J. Servain, J. A. Lorenz-zetti, and M. J. McPhaden (2005), Tropical instability waves at 0°N, 23°W in the Atlantic: A case study using Pilot Research Moored Array in the Tropical Atlantic (PIRATA) mooring data, *J. Geophys. Res.*, *110*, C08010, doi:10.1029/2005JC002941.

Haertel, P. T., and A. Fedorov (2012), The ventilated ocean, *J. Phys. Oceanogr.*, *42*, 141–164.

Haertel, P. T., and D. A. Randall (2002), Could a pile of slippery sacks behave like an ocean?, *Mon. Weather Rev.*, *130*, 2975–2988.

Haertel, P. T., and K. Straub (2010), Simulating convectively coupled Kelvin waves using Lagrangian overturning for a convective parameterization, *Q. J. R. Meteorol. Soc.*, *136*, 1598–1613.

Haertel, P. T., D. A. Randall, and T. G. Jensen (2004), Simulating upwelling in a large lake using slippery sacks, *Mon. Weather Rev.*, *132*, 66–77.

Haertel, P. T., L. Van Roekel, and T. Jensen (2009), Constructing an idealized model of the North Atlantic Ocean using slippery sacks, *Ocean Modell.*, *27*, 143–159.

Harlow, F. H. (1964), The particle-in-cell computing method for fluid dynamics, *Methods Comput. Phys.*, *3*, 319–343.

Hendon, H., M. C. Wheeler, and C. Zhang (2007), Seasonal dependence of the MJO-ENSO relationship, *J. Clim.*, *20*, 531–543.

Jensen T. G. (1996), Artificial retardation of barotropic waves in layered ocean models, *Mon. Weather Rev.*, *124*, 1272–1283.

Kennan S. C., and P. J. Flament (2000), Observations of tropical instability wave vortex, *J. Phys. Oceanogr.*, *30*, 2277–2301.

Kiladis, G. N., K. H. Straub, and P. T. Haertel (2005), Zonal and vertical structure of the Madden-Julian oscillation, *J. Atmos. Sci.*, *62*, 2790–2809.

Lin, J.-L., et al. (2006), Tropical intraseasonal variability in 14 IPCC AR4 climate models. Part I: Convective signals, *J. Clim.*, *19*, 2665–2690.

Lorenz, D. J., and D. L. Hartmann (2006), The effect of the MJO on the North American Monsoon, *J. Clim.*, *19*, 333–343.

Madden, R., and P. Julian (1972), Description of global-scale circulation cells in the tropics with a 40–50 day period, *J. Atmos. Sci.*, *29*, 1109–1123.

Madden, R., and P. Julian (1994), Observations of the 40–50 day tropical oscillation—A review, *Mon. Weather Rev.*, *122*, 814–837.

Maloney, E. D., and D. L. Hartmann (2000), Modulation of hurricane activity in the Gulf of Mexico by the Madden-Julian Oscillation, *Science*, *287*, 2002–2004.

Marshall, J., and T. Radko (2003), Residual-mean solutions for the Antarctic Circumpolar Current and its associated overturning circulation, *J. Phys. Oceanogr.*, *33*, 2341–2354.

McPhaden, M. J. (2004), Evolution of the 2002/03 El Niño, *Bull. Am. Meteorol. Soc.*, *85*, 677–695.

Monaghan, J. J. (1992), Smoothed particle hydrodynamics, *Annu. Rev. Astron. Astrophys.*, *30*, 543–574.

Schar, C., and P. K. Smolarkiewicz (1996), A synchronous and iterative flux-correction formalism for coupled transport equations, *J. Comput. Phys.*, *128*, 101–120.

Straub, K. H., and P. Haertel (2010), An analysis of convectively coupled Kelvin waves in 20 WCRP CMMIP3 global coupled climate models, *J. Clim.*, *23*, 3031–3056.

Van Roekel, L., T. Ito, P. Haertel, and D. Randall (2009), Lagrangian analysis of the meridional overturning circulation in an idealized ocean basin, *J. Phys. Oceanogr.*, *39*, 2175–2193.

Wu, M. L. C., S. Schubert, and N. E. Huang (1999), The development of the South Asian Summer Monsoon and the Intraseasonal Oscillation, *J. Clim.*, *12*, 2054–2075.

Yserentant, H. (1997), A particle model of compressible fluids, *Numer. Math.*, *76*, 111–142.

Zhang, C. (2005), Madden-Julian Oscillation, *Rev. Geophys.*, *43*, RG2003, doi:10.1029/2004RG000158.

P. T. Haertel, Department of Geology and Geophysics, Yale University, 210 Whitney Ave, New Haven, CT 06510, USA. (patrick.haertel@yale.edu)